Arch. Metall. Mater. **70** (2025), 4, 1863-1874

DOI: https://doi.org/10.24425/amm.2025.156273

X. LI[1,2,3,4], E. WU[1,2,3,4*], P. LIU[1,2,3*], W. PENG[1,2,3], J. LI[1,2,3,4], J. TANG[1,2,3], X. TANG[1,2,3], Z. XV[1,2,3], J. HOU[1,2,3], Y. ZHANG[1,2,3], B. ZHANG[5], S. CHEN[5]

NON-ISOTHERMAL KINETIC ANALYSIS OF MAGNESIUM SALT OXIDATION ROASTING PROCESS OF VANADIUM-TITANIUM MAGNETITE CONCENTRATE

Graphical abstract

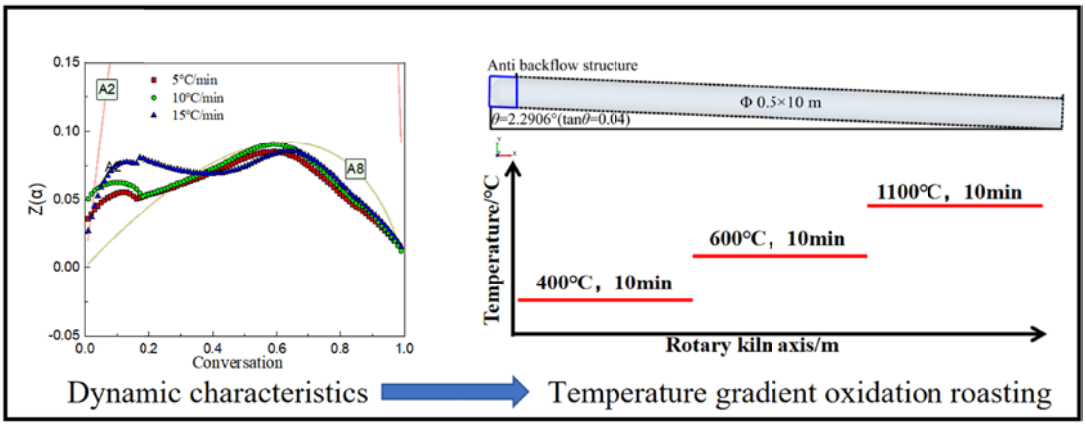

To enhance the recovery rate of vanadium from vanadium-titanium magnetite concentrate, we investigated a series of oxidation roasting reactions involving vanadium-titanium magnetite concentrate and magnesium oxide using non-isothermal kinetics. We employed four different model-free methods to calculate the apparent activation energy of the reactions over a temperature range of 396.2 to 836.6°C. Among these, the KAS method showed the best fitting accuracy, yielding an activation energy of 225.97 kJ/mol. This method was utilized to derive a stage reaction model and describe the kinetic mechanism. Our analysis confirmed that the A2 and A8 nucleation models were the dominant mechanisms throughout the entire reaction stage. Based on the derived kinetic mechanism, we propose strategies for enhancing reactivity through material pretreatment in the early reaction stage and employing a gradient temperature roasting strategy to increase the reaction temperature.

Keywords: Vanadium-titanium magnetite concentrate; MgO; oxidation roasting; dynamics

1. Introduction

Vanadium is an important rare metal that is widely used in various applications, including steel production, alloy materials, batteries, pigments, the chemical industry, and medicine [1-7]. Notably, in the growing sector of energy storage, vanadium redox flow batteries stand out as a new type of high-efficiency power conversion and energy storage device. They have significant potential in the vanadium market thanks to their safety, high charge and discharge efficiency, and environmental benefits

[1] VANADIUM AND TITANIUM COLLEGE OF PANZHIHUA UNIVERSITY, PANZHIHUA, SICHUAN 617000, CHINA
[2] SICHUAN PROVINCIAL KEY LABORATORY OF COMPREHENSIVE UTILIZATION OF VANADIUM AND TITANIUM RESOURCES, PANZHIHUA, SICHUAN 617000, CHINA
[3] SICHUAN SOLAR ENERGY UTILIZATION TECHNOLOGY INTEGRATED ENGINEERING LABORATORY, PANZHIHUA, SICHUAN 617000, CHINA
[4] STATE KEY TESTING LABORATORY OF VANADIUM & TITANIUM, PANZHIHUA 617000, SICHUAN, CHINA
[5] LB SICHUAN MINING AND METALLURGY CO., LTD, PANZHIHUA, SICHUAN 617000, CHINA

* Corresponding authors: wuenhui1026@126.com, tbagmo@126.com

[8-12]. Around 85% of vanadium is used in steel production to enhance the strength and toughness of steel, which limits its application in other fields [13-14]. To foster the development of vanadium in new energy storage and other sectors, further research is needed on efficient recovery methods for vanadium.

Currently, two primary methods exist for recovering vanadium from vanadium-titanium magnetite concentrate. The first method involves extracting vanadium from vanadium-rich steel slag, while the second method entails direct chemical extraction from the concentrate itself. Vanadium-rich steel slag is a valuable secondary mineral resource generated during the steelmaking process using vanadium-titanium magnetite concentrate. In industrial applications, vanadium is mainly extracted through secondary smelting of this steel slag. However, the production capacity of vanadium is closely tied to the capacity of steel production and its associated CO_2 emissions, which limits its application primarily to the steel industry [15]. Additionally, the vanadium recovered from steel slag has limited flexibility and is heavily reliant on the blast furnace converter process [16-18]. To diversify vanadium production sources and enhance the growth of the all-vanadium flow battery industry, it is essential to conduct in-depth research on the direct vanadium extraction process from vanadium-titanium magnetite concentrate. This process involves breaking down the phase structure of the concentrate by adding additives and conducting an oxidizing roast. During this step, low-valent vanadium in the ore is converted into high-valent vanadate. Subsequently, a vanadium-rich solution is obtained through leaching and filtration, and the vanadium is then precipitated and calcined to produce high-grade V_2O_5. This direct extraction method has gained attention due to its low energy consumption, short processing time, and high recovery rate. The process is divided into four main stages: oxidation roasting, leaching, vanadium precipitation, and calcination. The efficiency of vanadium recovery is significantly influenced by the amount of soluble vanadate produced at the end of the oxidation roasting phase. As such, oxidation roasting is a crucial step in the entire direct vanadium extraction process.

Luo studied the oxidation roasting performance of sodium salt in vanadium-titanium magnetite concentrate. It was found that sodium metavanadate soluble in water was formed under the conditions of Na_2CO_3 addition of 7.5%, heating rate of 10°C/min, roasting temperature of 850°C and roasting time of 4h, and its roasting conversion rate (oxidation degree) was as high as 92% [19]. It is proved that the roasting additive has a gain effect on the oxidation roasting, but the sodium salt consumption is too large, which cannot be recycled in the whole vanadium extraction process and hinders the subsequent recovery of other precious metals [20-23]. Calcification roasting also has a similar effect, but some problems cannot be recycled. However, it will produce acid-soluble calcium ferrite, resulting in a higher iron loss rate, and the residual sulfur ions cause pollution to the environment [24-27]. In terms of roasting conversion efficiency, the addition of magnesium salts (MgO, $MgCO_3$, $Mg(OH)_2$) to the vanadium-titanium magnetite concentrate can also effectively destroy the mineral phase structure after oxidation roasting, optimize the roasting effect, and react to form magnesium vanadate and magnesium metavanadate that are soluble in acid. However, unlike sodium salt additives, magnesium salts can be recycled in the process of vanadium precipitation, In the whole process of vanadium extraction, selective recovery can be achieved, and the subsequent recovery of elements such as Ti, Al and Fe in vanadium-titanium magnetite concentrate can be achieved to achieve comprehensive utilization of resources and enhances overall process efficiency [28-30]. so that the whole vanadium extraction process can achieve green closed-loop, energy saving and emission reduction, which is of great significance to the development of vanadium extraction technology.

In this work, the non-isothermal kinetics analysis of the magnesium salt roasting process of vanadium-titanium magnetite concentrate was carried out to determine the rate control steps and reveal the reaction mechanism, which provided theoretical guidance for the direct extraction of vanadium from vanadium-titanium magnetite concentrate by magnesium salt roasting.

2. Experimental

2.1. Sample

The Vanadium Titanomagnetite Concentrate (VTMC) used in this study was from LB Sichuan Mining and Metallurgy Co., Ltd., with magnesium oxide (analytically pure).

The chemical composition analysis of VTMC is shown in TABLE 1 (with the mass fraction of Fe_3O_4 and V_2O_5 as the calculated value). Iron oxide and titanium oxide account for about 85% of its content, and contain silicon oxide and magnesium oxide, as well as trace impurity elements such as S, Ca, Cr, and Mn.

The XRD spectrum and SEM images of vanadium-titanium magnetite concentrate are shown in Fig. 1. TABLE 2 shows the atomic ratio and mass ratio of Fe, Ti, O, and V in this region. As shown in Fig. 1(a), it can be seen that the phase is mainly composed of Fe_3O_4 and $FeTiO_3$, corresponding to the analysis of the composition content in TABLE 1. As shown in Fig. 1(b-f) and TABLE 2, The overall appearance of the area is a grid-like structure, and the Fe element content is high and evenly distributed on the ore surface. Among them, the Ti element is unevenly distributed in strips; the content of V element is less.

TABLE 1

Analysis of the chemical composition of VTMC

Ore	TFe	Fe_3O_4	FeO	TiO_2	MgO	SiO_2	Al_2O_3	CaO	V_2O_5	Cr_2O_3	NiS	MnO
wt.%	55.37	68.27	8.4	9.34	3.27	3.88	2.46	0.85	0.58	0.64	0.12	0.26

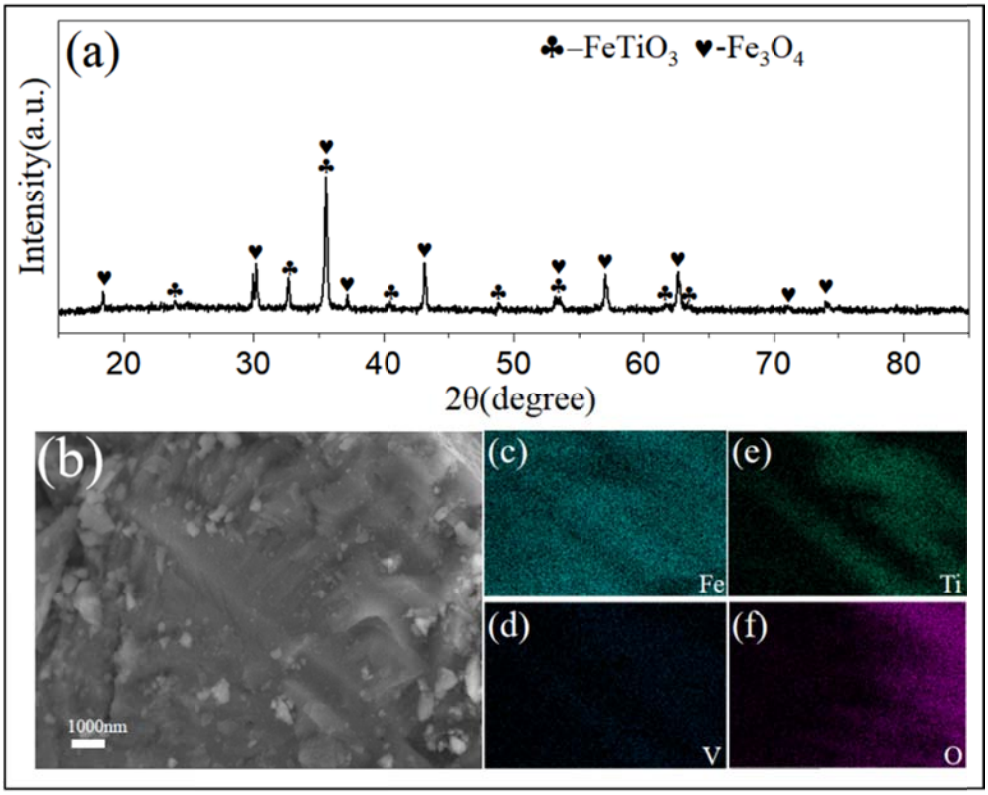

Fig. 1. XRD patterns (a), SEM and EDS of VTMC (b-f)

TABLE 2

Atomic ratio and mass ratio of Fe, Ti, O, and V

Element	Fe	Ti	O	V
wt.%	66.27	9.61	14.56	0.52
Atomic%	51.15	8.09	36.18	0.41

2.2. Experimental method

Firstly, the Vanadium Titanomagnetite Concentrate (VTMC: MgO, 100:6) was weighed in proportion to MgO. After uniform mixing, the mixture was placed in a tube furnace and oxidized, and calcined in an air atmosphere for 2 h. The calcination temperature range was from room temperature to 1100°C. Finally, the calcined product was obtained by natural cooling to room temperature in air atmosphere. The experimental process is shown in Fig. 2.

2.3. Thermogravimetric experiments

Thermogravimetric experiments were performed by TGA (Netzsch STA 449 F3) to obtain TG and DTG curves for kinetic

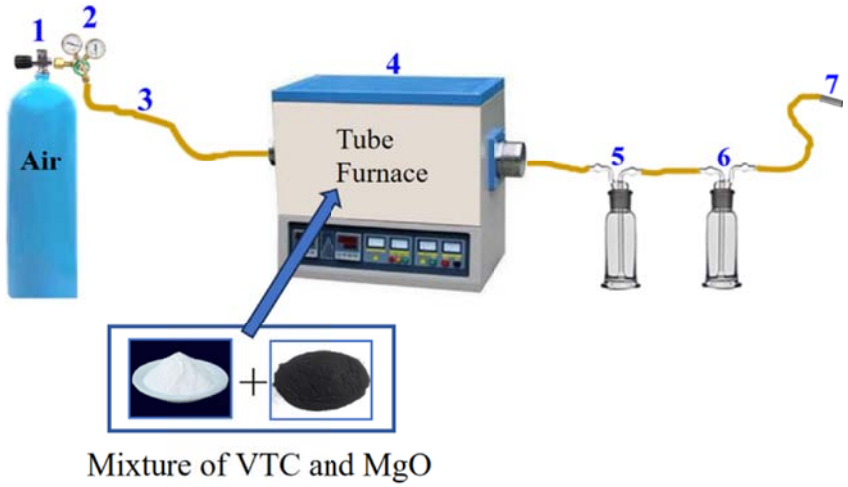

Fig. 2. Roasting flow chart. (1 – Drying air, 2 – Flowmeter (air flow rate 60 mL/min), 3 – Rubber hoses, 4 – Tubular muffle furnaces, 5 – Meng's washing bottles (anti-backflow suction), 6 – Meng's washing bottles (water), 7 – Tail gas (discharged into the air)

analysis. The temperature and sensitivity were calibrated using calcium oxalate monohydrate (dehydration step at 120°C, decomposition at 550°C). The balance sensitivity was ±0.2 μg, and buoyancy effects were corrected via baseline subtraction under identical experimental conditions. DSC measurements used a TA Instruments Q200, calibrated with indium ($\Delta Hfus$ = 28.4 J/g ± 0.5 J/g) and sapphire for heat capacity. A homogeneous mixture of vanadium-titanium magnetite concentrate and magnesium oxide (VTMC: MgO, 100:6) was used as a raw material. Each group of samples was weighed 8 mg and heated from room temperature to 1100°C at 5,10, and 15°C / min, respectively. The airflow rate was 60 mL/min.

2.4. Apparent activation energy

The model-free method is considered to be a reliable method to obtain the apparent activation energy E_a [31-35] of complex and multi-reaction processes without knowing the expression of the relevant reaction mechanism function $g(\alpha)$. he calculation process is described in detail in [36]. The four model-free methods listed in TABLE 3 are all iso conversional methods, and the apparent activation energy E_a is calculated based on the TG / DTG data at different heating rates (three) in the reaction temperature range.

TABLE 3

Common model-free methods and the corresponding equations

Method	Equation	Ref.
Flynn Wall Ozawa (FWO)	$\ln\beta = \ln\left[\frac{AE_a}{Rg(\alpha)}\right] - 5.331 - 1.052\frac{E_a}{RT}$	[38-41]
Starink	$\ln\left(\frac{\beta}{T^{1.92}}\right) = Const. - 1.0008\left(\frac{E_a}{RT}\right)$	[35]
Friedman	$\ln\left[\beta\left(\frac{d\alpha}{dT}\right)\right] = \ln\left[Af(\alpha)\right] - \frac{E_a}{RT}$	[42]
KAS	$\ln\left[\frac{\beta}{T_{peak}^2}\right] = \ln\left[-\frac{AR}{E_a}f'(\alpha_m)\right] - \frac{E_a}{RT_{peak}}$	[35,38]

2.5. Dominant mechanism function

The conversion rate α in the oxidation roasting process can be derived from the TG data by Eq. (2).

$$\alpha = \frac{m_0 - m_t}{m_0 - m_\infty} \qquad [29]\ (1)$$

In Eq. (1), the initial mass of the sample at the beginning of the reaction interval corresponding to the TG curve is m_0, the final mass of the sample at the end of the reaction interval is m_∞, and the mass of the remaining sample at t in the reaction process is m_t.

Combining the model-free method with the $Z(\alpha)$ rincipal function method, the dominant mechanism function of the oxidation roasting process can be determined. Using the model fitting method, the range of possible $g(\alpha)$ listed in TABLE 4 is reduced by selecting $g(\alpha)$ with R^2 close to 1. The A and E_a [39-41] of each $g(\alpha)$ were calculated by linear fitting using the Coats-Redfern equation [37-38].

$$\ln\left[\frac{g(\alpha)}{T^2}\right] = \ln\left[\frac{AR}{\beta E_a}\right] - \frac{E_a}{RT} \qquad [29]\ (2)$$

By comparing the theoretical – $Z(\alpha)$ function value and the experimental – $Z(\alpha)$ function value with the change trend of α under different heating rates of each $g(\alpha)$, the dominant mechanism function is further determined.

$$Z(\alpha) = f(\alpha)\, g(\alpha) \qquad [29]\ (3)$$

$$Z(\alpha) = \frac{\pi(u)\left(\frac{d\alpha}{dt}\right)T}{\beta} = \pi(u)\left(\frac{d\alpha}{dT}\right)T \qquad [29]\ (4)$$

$$\pi(u) = \frac{u^3 + 18u^2 + 86u + 96}{u^4 + 20u^3 + 120u^2 + 240u + 120} \qquad (5)$$

$$u = \frac{E_a}{RT} \qquad (6)$$

Eq. (3) is the theoretical calculation expression of $Z(\alpha)$, and Eq. (4) is the experimental calculation expression of $Z(\alpha)$. The E_a in Eq. (6) is calculated by the model-free method.

2.6. Material characterization

EDS Sample Preparation Method: The samples were prepared by mixing epoxy resin and its curing agent at a mass ratio of 2:1. The mixture was stirred uniformly in the same direction for 2-3 min until fully homogenized. Subsequently, it was poured into a cold-mounted mold containing the pre-loaded sample. The curing process was conducted at 25°C for 6-10 h. After demolding, the sample was polished to a smooth and flat mirror for subsequent analysis. EDS analysis was conducted using an Oxford Instruments X-MaxN 80 detector coupled to a ZEISS Sigma 300 scanning electron microscope, the EDS system was calibrated using NIST-certified reference materials (Cu, Fe, Al) before measurement.

The phase of vanadium-titanium magnetite concentrate was detected by X-ray diffraction analysis (XRD dynamic 500, Cu Kα radiation at 40 kV and 40 mA)with a step size of 0.02° 2θ and a counting time of 2 s/step. The instrumental broadening was calibrated using a LaB6 standard (NIST SRM 660a). The surface morphology and element distribution of vanadium-titanium magnetite concentrate and magnesium oxide before and after roasting were observed by scanning electron microscope (ZEISS Sigma 300).

TABLE 4

Kinetic models commonly used in oxidation roasting

Model Accelerating type	Symbol	Differential form $f(\alpha)$	Integral form $g(\alpha)$
Exponential law	E1	α	$\ln\alpha$
Nucleation models			
Avarami-Erofe'ev	A2	$2(1-\alpha)[-\ln(1-\alpha)]^{1/2}$	$[-\ln(1-\alpha)]^{1/2}$
Avarami-Erofe'ev	A3	$3(1-\alpha)[-\ln(1-\alpha)]^{2/3}$	$[-\ln(1-\alpha)]^{1/3}$
Avarami-Erofe'ev	A4	$4(1-\alpha)[-\ln(1-\alpha)]^{3/4}$	$[-\ln(1-\alpha)]^{1/4}$
Avarami-Erofe'ev	A5	$2/3(1-\alpha)[-\ln(1-\alpha)]^{-1/2}$	$[-\ln(1-\alpha)]^{3/2}$
Avarami-Erofe'ev	A6	$1/2(1-\alpha)[-\ln(1-\alpha)]^{-1}$	$[-\ln(1-\alpha)]^{2}$
Avarami-Erofe'ev	A7	$1/3(1-\alpha)[-\ln(1-\alpha)]^{-2}$	$[-\ln(1-\alpha)]^{3}$
Avarami-Erofe'ev	A8	$1/4(1-\alpha)[-\ln(1-\alpha)]^{-3}$	$[-\ln(1-\alpha)]^{4}$
Decelerating type			
Geometrical contraction models			
Contracting area	R2	$2(1-\alpha)^{1/2}$	$1(1-\alpha)^{1/2}$
Contracting volume	R3	$3(1-\alpha)^{2/3}$	$1(1-\alpha)^{1/3}$
Diffusion models			
Parabolic law, one-dimensional diffusion	D1	$1/2\alpha$	α^2
Valesitwo-dimensional diffusion	D2	$[-\ln(1-\alpha)]^{1}$	$(1-\alpha)\ln(1-\alpha)+\alpha$
Jander, three-dimensional diffusion	D3	$(3/2)(1-\alpha)^{2/3}[1-(1-\alpha)^{1/3}]^{-1}$	$[1-(1-\alpha)^{1/3}]^2$
Ginstling-Brounshtein, three-dimensional diffusion	D4	$(3/2)[(1-\alpha)^{-1/3}-1]^{-1}$	$1-2\alpha/3-(1-\alpha)^{2/3}$
Z-L-T equation, three-dimensional diffusion	D5	$(3/2)(1-\alpha)^{4/3}[(1-\alpha)^{1/3}-1]^{-1}$	$[(1-\alpha)^{1/3}-1]^2$
Reaction-order models			
First order	F1	$1-\alpha$	$-\ln(1-\alpha)$
Second order	F2	$(1-\alpha)^2$	$(1-\alpha)^{-1}-1$
Third order	F3	$2(1-\alpha)^3$	$[(1-\alpha)^{-2}-1]/2$

3. Results and discussion

3.1. Thermodynamics calculation

In the process of magnesium salt roasting reaction, the main phase in the vanadium-titanium magnetite concentrate reacts with the roasting additive MgO as shown in Eqs. (7)-(9). When there are Si and V oxides, the chemical reactions that may occur are shown in Eqs. (10)-(12). In essence, the oxidation roasting reaction is the oxidation reaction of the main phase in the vanadium-titanium magnetite concentrate. The most important thing is to first destroy the silicate phase on the surface of the vanadium-titanium magnetite concentrate so that the vanadium-iron spinel is oxidized by air and converted into vanadate which is soluble in acid. This process involves the diffusion of Mg^{2+} and O^2, and the reaction produces vanadate and hematite-based solid products and a small amount of SO_x gas (Eq. (13)). The thermodynamic data calculated based on HSC 6 software are shown in Fig. 3. According to Fig 3, ΔG of formula 8 is less than 0, indicating that magnetite in vanadium-titanium magnetite concentrate will be converted into hematite during oxidation. The main reaction ΔG and ΔH of the whole roasting process

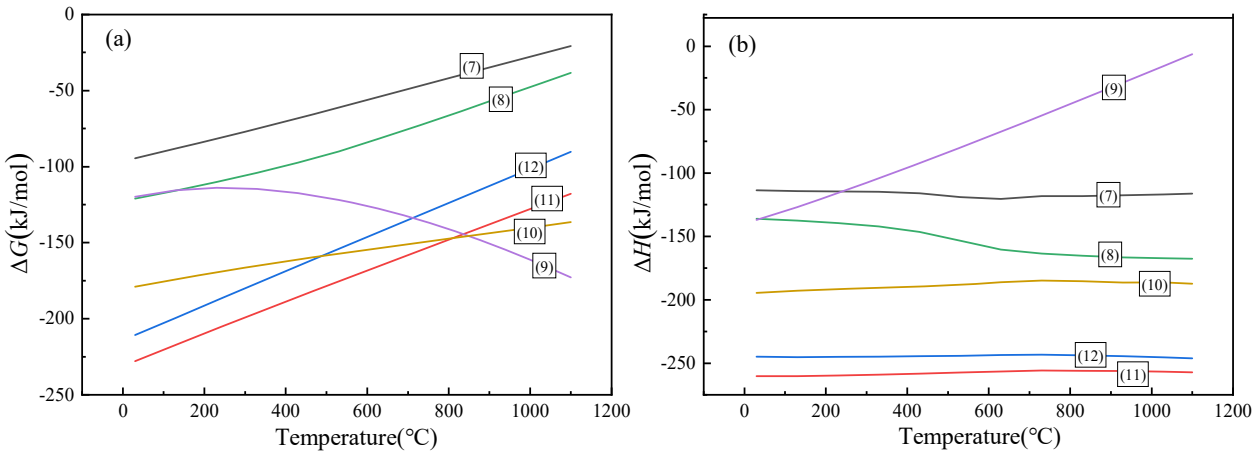

Fig. 3. ΔG – Temperature curves (a) and ΔH – Temperature curves (b) of reactions related to the VTMC and MgO

are less than 0, and the reaction is exothermic. The increase in temperature is not conducive to the reaction.

$$4Fe_3O_4 + O_2 = 6Fe_2O_3 \quad [29]\ (7)$$

$$4Fe_3O_4 + 6MgO + O_2 = 6MgFe_2O_4 \quad [29]\ (8)$$

$$4FeTiO_3 + 6MgO + O_2 = 4MgTiO_3 + 2MgFe_2O_4 \quad (9)$$

$$2Fe_2SiO_4 + 2MgO + O_2 = 2Fe_2O_3 + 2MgSiO_3 \quad (10)$$

$$0.8FeV_2O_4 + 1.6MgO + O_2 = 0.8Mg_2V_2O_7 + 0.4Fe_2O_3 \quad (11)$$

$$0.8FeV_2O_4 + 0.8MgO + O_2 = 0.8MgV_2O_6 + 0.4Fe_2O_3 \quad (12)$$

$$NiS + O_2 = NiO + SO_x \quad (13)$$

3.2. Thermogravimetric results

The TG and DTG curves of the calcined products at different heating rates are shown in Fig. 4(a) and Fig. 4(b), respectively. As the temperature increases from room temperature to 1100℃, the whole roasting process can be divided into four stages. Combined with the composition and thermodynamic data of vanadium-titanium magnetite concentrate; The first stage (30-396℃) corresponds to the removal weight loss of free water and crystal water; The second stage (396.2-836.6℃) corresponds to the weight gain of the oxidation reaction process; The third stage of weight loss may be related to the formation of SO_X gas and the vaporization removal of ionic state V [43], the vaporization removal of ionic state V means that a part of the V mass loss will be caused during the roasting process. The quality of the fourth stage (temperature range) remains unchanged, and the oxidation reaction in the roasting process ends.

3.3. Apparent activation energy E_a calculation by model-free method

The results of the conversion rate and activation energy calculated by four model-free methods are shown in Fig. 5. Fig. 5(a) is the change trend of conversion rate α with temperature T. It can be seen from Fig. 5(a) that the conversion rate increases with the increase of temperature at different heating rates. However, at the same temperature, the conversion rate decreases with the increase of heating rate. At a fixed temperature, the activation energy can be calculated by the model-free method. The calculation results of FWO model-free method [34-36] at different conversion rates are shown in Fig. 5(b), and the negative slope is the apparent activation energy E_a. It can be found that with the increase of conversion rate, E_a increases from 82.44 kJ·mol^{-1} to 580.34 kJ·mol^{-1}.

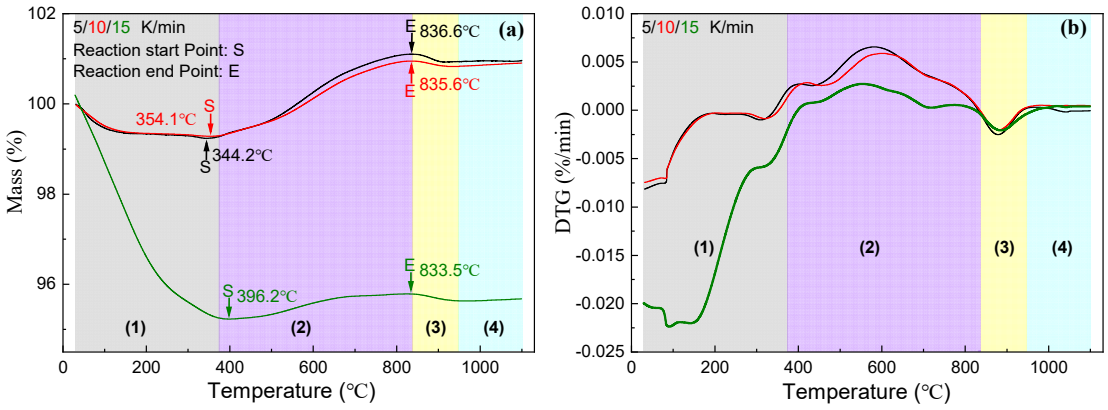

Fig. 4. TG (b) and DTG (b) curves of samples at different heating rates

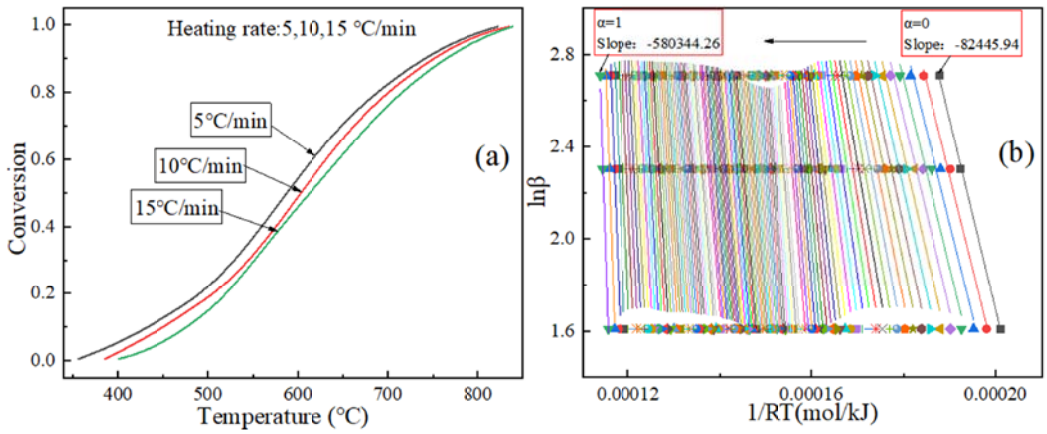

Fig. 5. The growth trend of conversion rate at different heating rates (a). Liner fitting calculation of activation energy at different conversions by FWO model-free method (b)

The apparent activation energy E_a calculated by the four model-free methods based on TABLE 3 is shown in Fig. 6. The fitting results obtained by the four model-free methods are all good. The E_a values calculated by FWO, Starink, Friedman and KAS are not much different, all fluctuate around the average value and show an upward trend. In fact, the activation energy calculated by the Friedman method (592.63 kJ·mol^{-1}) is slightly higher than the other three calculations. In the calculation process of the Friedman method, the $d\alpha/dT$ data calculated by the DTG curve is used, while the results of the other three methods are obtained by using the temperature power index data and the adjustment coefficient. TABLE 5 shows the activation energy values and adjusted coefficient of determination (adjusted R^2) calculated by the four model-free methods. Considering that the adjusted R^2 of KAS is closer to 1 and the fitting effect is better, the E_a-KAS method (225.97 kJ/mol) is used as the intermediate parameter to derive the kinetic reaction mechanism.

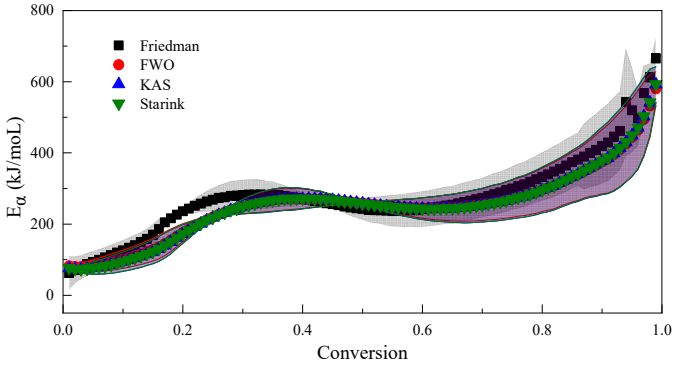

Fig. 6. E_a calculated by model-free methods listed in TABLE 3

3.4. Dominant function determination by Model-fitting method

The kinetic models commonly used in the oxidation roasting process are shown in TABLE 4. The fitting results of the heating rate of 5°C / min are shown in Fig. 7. From Fig. 7, it can be seen that the A8, A7, A6, A5, and D5 models have better fitting effects, and Adj-R^2 is greater than 0.97. Table 6 shows the specific parameter values of the fitting results. By comparing the activation energy values of E_a-KAS and E_a-model methods, a model with better fitting effect can be determined. The two models of A8 and A7 are close to the values of E_a-KAS (225.97 kJ/mol), and the deviations from E_a-KAS are 14.32% and –15.81%, respectively. The scope of application of the reaction model can be reduced by comparing the fitting results of the model method. $Z(\alpha)$ master-plot method will further confirm the exact mechanism of the reaction process through the relevant kinetic model.

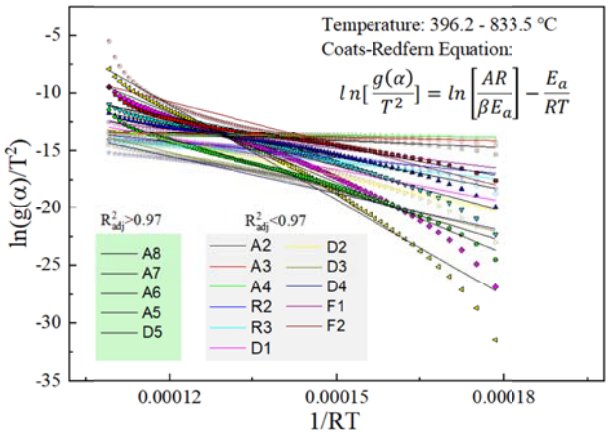

Fig. 7. Model fitting results of heating rates (5°C·min^{-1})

3.5. Mechanism analysis by $Z(\alpha)$ master-plot method

The curves in Fig. 8 are the $Z(\alpha)$-model and $Z(\alpha)$-experiment. Fig. 8(a) shows the fitting results of all models, and Fig. 8(b) shows the best-fitting model. The point values of $Z(\alpha)$-experiment at three different heating rates have almost the same trend with the conversion rate, but the trend does not conform to the curve drawn by a single model. As the reaction proceeds, the dominant model changes. When the conversion rate is lower than 10%, the experimental data is close to the A2 model. When the conversion rate increases to 20%, it gradually transitions to the A8 model curve. This is because the magnesium oxide reacts with the material surface in a multi-point form, destroying the crystal structure of the material surface. As the conversion rate increases, the reaction core grows and gradually diffuses around, forming a phase boundary with other reaction points, blocking the diffusion channel of oxygen until the end of the reaction. The whole

TABLE 5

Calculated activation energy at different conversions by the model-free methods

Conversion	Friedman		FWO		KAS		Starink	
	E_a (kJ·mol^{-1})	Adj. R^2	E_a (kJ·mol^{-1})	Adj. R^2	E_a (kJ·mol^{-1})	Adj. R^2	E_a (kJ·mol^{-1})	Adj. R^2
0.1	126.13	0.91	85.95	0.91	75.93	0.99	74.63	0.93
0.2	235.94	1.00	176.11	0.95	172.36	0.95	172.74	0.95
0.3	281.67	0.96	249.42	0.99	248.89	0.99	249.24	0.99
0.4	270.59	0.99	271.22	0.98	271.33	0.98	271.68	0.98
0.5	242.35	0.97	258.89	1.00	257.87	1.00	258.24	1.00
0.6	241.86	0.92	245.35	0.97	243.10	0.97	243.51	0.97
0.7	273.44	0.92	254.89	0.94	242.61	0.93	253.03	0.93
0.8	332.97	0.92	296.47	0.92	295.70	0.91	296.11	0.91
Average	250.62	0.949	229.79	0.957	225.97	0.965	227.39	0.957

TABLE 6

Kinetic parameters obtained by different reaction models

Model	Variable	5°C·min^{-1}	10°C·min^{-1}	15°C·min^{-1}	Average
A2	lnA(min^{-1})	1.90	0.93	0.24	1.02
	E_a(kJ·mol^{-1})	18.10	19.98	21.95	20.01
	Adj. R^2	0.96	0.94	0.93	0.94
A3	lnA(min^{-1})	4.20	3.26	2.61	3.36
	E_a(kJ·mol^{-1})	7.50	8.64	9.84	8.66
	Adj. R^2	0.87	0.86	0.85	0.86
A4	lnA(min^{-1})	6.14	5.07	4.35	5.19
	E_a(kJ·mol^{-1})	2.20	2.98	3.79	2.99
	Adj. R^2	0.46	0.53	0.56	0.52
R2	lnA(min^{-1})	0.93	2.03	2.84	1.93
	E_a(kJ·mol^{-1})	40.74	44.08	47.50	44.11
	Adj. R^2	0.94	0.93	0.91	0.93
R3	lnA(min^{-1})	1.07	2.19	3.03	2.10
	E_a(kJ·mol^{-1})	43.55	47.11	50.80	47.15
	Adj. R^2	0.95	0.95	0.93	0.94
D1	lnA(min^{-1})	6.87	8.21	9.24	8.11
	E_a(kJ·mol^{-1})	80.93	86.83	92.67	86.81
	Adj. R^2	0.91	0.89	0.87	0.89
D2	lnA(min^{-1})	7.72	9.13	10.25	9.03
	E_a(kJ·mol^{-1})	89.40	95.95	102.59	95.98
	Adj. R^2	0.94	0.93	0.91	0.93
D3	lnA(min^{-1})	8.25	9.75	11.00	9.67
	E_a(kJ·mol^{-1})	100.80	108.24	115.98	108.34
	Adj. R^2	0.97	0.96	0.95	0.96
D4	lnA(min^{-1})	6.88	8.32	9.48	8.23
	E_a(kJ·mol^{-1})	93.11	99.95	106.94	100.00
	Adj. R^2	0.95	0.94	0.93	0.94
F1	lnA(min^{-1})	3.36	4.53	5.45	4.45
	E_a(kJ·mol^{-1})	49.91	53.97	58.28	54.05
	Adj. R^2	0.95	0.97	0.97	0.96
F3	lnA(min^{-1})	13.37	15.01	16.56	14.98
	E_a(kJ·mol^{-1})	106.21	114.71	124.66	115.19
	Adj. R^2	0.88	0.88	0.90	0.89
A8	lnA(min^{-1})	30.44	32.93	35.28	32.88
	E_a(kJ·mol^{-1})	240.77	257.96	276.27	258.33
	Adj. R^2	0.99	0.98	0.98	0.98
A7	lnA(min^{-1})	21.63	23.68	25.55	23.62
	E_a(kJ·mol^{-1})	177.15	189.96	203.61	190.24
	Adj. R^2	0.99	0.98	0.98	0.98
A6	lnA(min^{-1})	12.68	14.29	15.68	14.22
	E_a(kJ·mol^{-1})	113.53	121.97	130.95	122.15
	Adj. R^2	0.99	0.98	0.97	0.98
A5	lnA(min^{-1})	8.11	9.50	10.65	9.42
	E_a(kJ·mol^{-1})	81.72	87.97	94.62	88.10
	Adj. R^2	0.98	0.98	0.97	0.98
D5	lnA(min^{-1})	13.06	14.79	16.34	14.73
	E_a(kJ·mol^{-1})	128.31	137.91	148.35	138.19
	Adj. R^2	0.99	0.99	0.98	0.99
F2	lnA(min^{-1})	7.88	9.26	10.46	9.20
	E_a(kJ·mol^{-1})	74.88	80.91	87.70	81.16
	Adj. R^2	0.95	0.95	0.96	0.95

reaction process is dominated by a two-stage gas-solid nucleation diffusion mechanism. When the conversion rate is less than 10%, for different heating rate curves, the temperature corresponding to the conversion rate of 10% is 435.9-478.6°C. The reaction rate is slow, and the process is mainly controlled by the nucleation model (A2). With the increase of temperature, the conversion rate

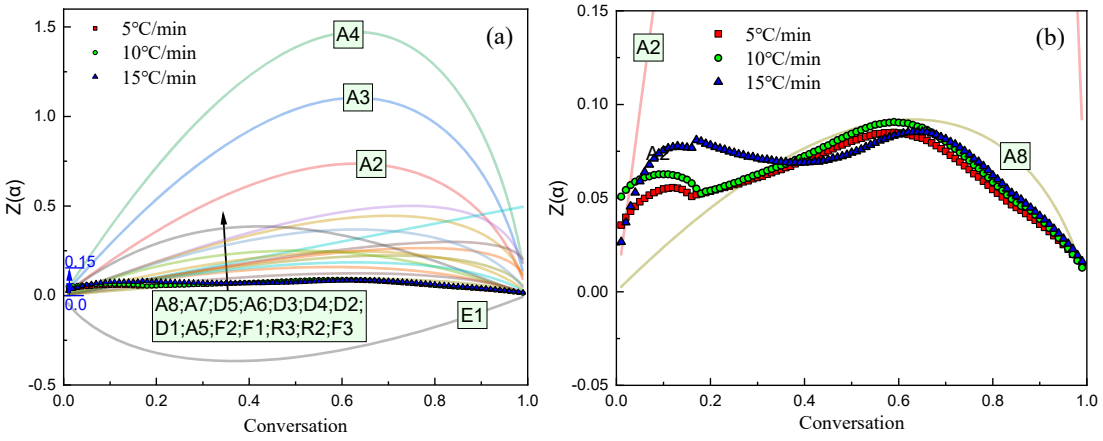

Fig. 8. Comparison of the experimental curves with theoretical curves at different heating rates (a), models with better fitting effects (b)

(>20%) increases. Due to the destruction of the lattice structure of the material, the exposed ferrovanadium spinel reacts with magnesium oxide to form soluble magnesium vanadate. The reaction process is controlled by the nucleation model (A8). From the above analysis process, it can be concluded that the dominant model of the oxidation roasting process is two nucleation models (A2, A8). Therefore, the pretreatment of the materials before the reaction, such as mechanical activation and increasing the specific surface area of the materials, can enhance the reactivity and improve the early multinuclear reaction process. In the later stage of the reaction, the reaction temperature control strategy will be more effective for the dominant A8 model. To maintain the nucleation strength and grain size during the roasting process, the stepped temperature roasting should be adopted. The oxidation reaction rate of the whole roasting reaction is faster between 400°C and 800°C, and the number of nucleation of the multi-point reaction can be increased by roasting at 400°C for 10 min. Roasting at 600°C for 10 minutes can promote the growth of core reaction sites and improve the strength of high-valence iron oxides. Roasting at 1100°C for 10 minutes at the endpoint of the reaction can further promote the roasting reaction and improve the oxidation degree of the roasted material by allowing oxygen to penetrate from the pores between the reaction points.

3.6. Morphology analysis after oxidation roasting

Fig. 9 presents SEM images of calcined products at different heating rates. As shown in Fig. 9(a), distinct phase boundaries are formed between granular Fe_2O_3 particles, indicating that oxidative roasting promotes the growth of multi-nucleation site reactions. After the reaction, most reactive sites remain

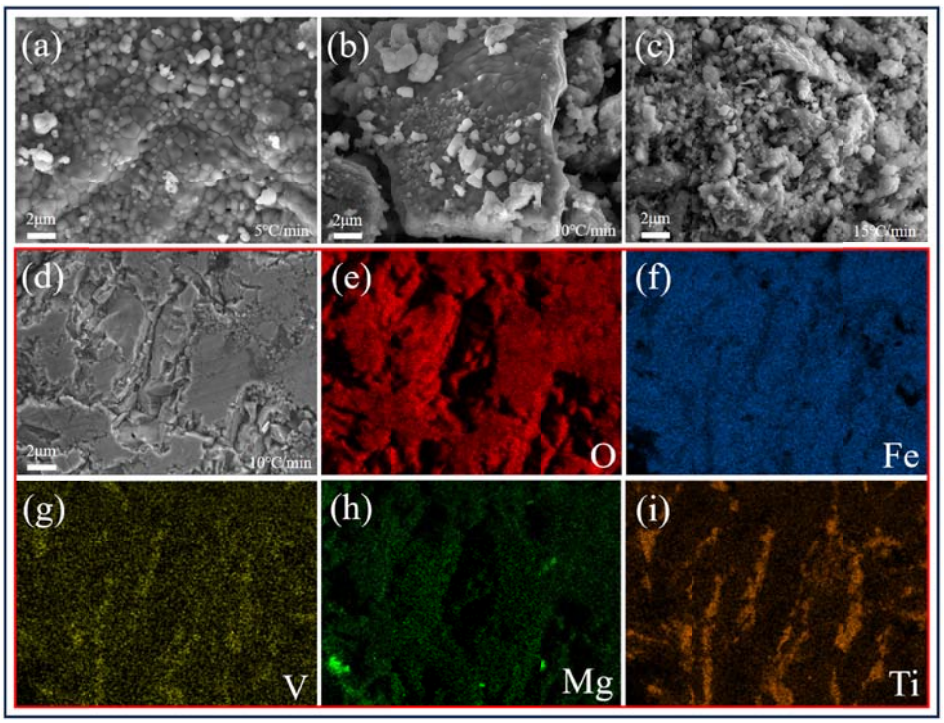

Fig. 9. SEM micrograph of calcined products at different heating rates, 5°C/min (a), 10°C/min (b), 15°C/min (c), 10°C/min (d), EDS-10°C/min (e-i)

unclosed, generating cracks or pores at the phase boundaries. These structural features significantly enhance the specific surface area of the roasted products, facilitating the adsorption of additional O_2 molecules within the interfacial gap channels or pores. In Fig. 9(b), irregular angular morphology and fragmented features are observed in the granular structures. The collapse of phase boundaries likely obstructs the interfacial gap channels, resulting in reduced structural continuity, as illustrated in Fig. 9(c), the growth of multi-nucleation sites in granular Fe_2O_3 is not confined to planar orientations. Instead, reactive sites develop into an irregular three-dimensional framework with abundant porosity. This phenomenon arises from the limited growth time of reactive sites under accelerated heating rates, which restricts particle size evolution. Consequently, the interfacial gap channels between phase boundaries expand, ultimately forming a disordered porous architecture. The SEM images and corresponding EDS elemental mapping results of the polished sample was shown in Fig 9(d-i). The distributions of V and Mg are highly consistent, indicating their association in the same phase. Notably, localized Mg enrichment is observed, likely caused by the grinding process disrupting the original mineral phase structure and exposing unreacted regions. In contrast, Ti exhibits an inhomogeneous, striated distribution pattern.

3.7. Process flow

Fig. 10 is the optimized process step diagram. Firstly, the mixture of MgO and VTMC was dried and put into planetary ball mill. Then the stepped temperature roasting is used to promote the full oxidation of the mixture; finally, after a series of processes such as acid leaching and vanadium extraction, the finished product V_2O_5 can be obtained. By optimizing the two stage process steps, the roasting oxidation effect can be effectively improved. Before the roasting reaction, the mixture of vanadium-titanium magnetite concentrate and magnesium oxide can be ball milled to reduce its particle size, increase its specific surface area and enhance its reactivity. Gradient temperature oxidation roasting was used during roasting, and the strength of the reaction product was improved by holding at 400°C, 600°C and 1100°C for 10 min, respectively.

4. Conclusion

In this study, non-isothermal roasting kinetics was used to study the roasting kinetics of the mixture of vanadium-titanium magnetite concentrate and magnesium oxide. The results indicate that two distinct mass loss stages occurred during the entire roasting process. The first stage corresponds to the removal of free water and water of crystallization, with a temperature range of 30-396.2°C.The second weight loss may be caused by the formation of SO_X gas and the vaporization of ionic state V, and the temperature range is 833.5-945.2°C. Four model-free methods were used to calculate the activation energy of the process, among which E_a-KAS (225.97kJ / mol) had the best fitting accuracy. Therefore, the E_a-KAS method is used as an intermediate parameter to derive the kinetic reaction mechanism. The results show that the experimental data are close to the A2 model when the conversion rate is less than 10%. When the conversion rate increases to 20%, it gradually transitions to the A8 model curve. The whole reaction process is dominated by the two-stage gas-solid nucleation diffusion mechanism, which is controlled by the two-stage nucleation model. Based on the previous kinetic analysis, the pretreatment of the material before the roasting stage and a certain degree of ball milling to change the particle size can improve the multi-core point reaction process dominated by A2 in the early stage of the reaction. The control of the reaction

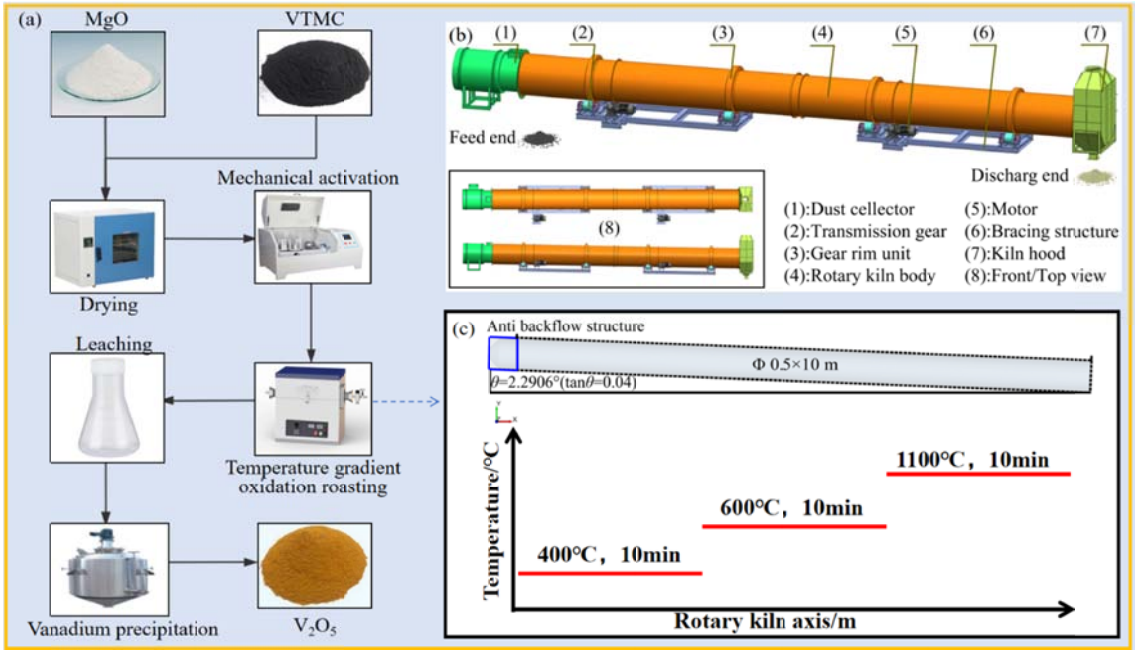

Fig. 10. Process flow diagram (a), Rotary kiln model (b), Temperature gradient oxidation roasting (c)

temperature can improve the nucleation process dominated by A8 in the later stage of the reaction. The number of nucleation of the multi-point reaction can be increased by roasting at 400℃ for 10 min; Roasting at 600℃ for 10 minutes can promote the growth of core reaction sites and improve the strength of high-valence iron oxides; Roasting at 1100℃ for 10 minutes at the endpoint of the reaction can further promote the roasting reaction and improve the oxidation degree of the roasted material by allowing oxygen to penetrate from the pores between the points.

Acknowledgments

This work was supported by Project of Panxi Strategic Resource Innovation and Development (LB-SK-HT23-0432), Project of Sichuan Provincial Key Laboratory of Material Corrosion and Protection (2022CL31), Project of Key Laboratory of Green Chemistry of Sichuan Institutes of Higher Education (LYJ2102). Project of Sichuan Province Key Laboratory of Higher Education Institutions for Fine Chemical Additives and Surfactant (2023JXY01), Project of Application and Solar Technology Integration Sichuan Provincial Key Laboratory of University Program (SN240104), Project of PZHU Graduate Student Innovation Program (y2024016), Project of Vanadium and Titanium Resource Comprehensive Utilization Key Laboratory of Sichuan Province (2024FTSZ04), Project supported by the Natural Science Foundation of Sichuan, China(Grant No.2025ZNSFSC0375) and Project of Sichuan Province Key Laboratory of Higher Education Institutions for Comprehensive Development and Utilization of Industrial Solid Waste in Civil Engineering (SC-FQWLY-2021-Z-08).

REFERENCE

[1] M. Attah, F. Hildor, D. Yilmaz, H. Leion, Vanadium recovery from steel converter slag utilised as an oxygen carrier in oxygen carrier aided combustion (OCAC). Journal of Cleaner Production **293**, 126159 (2021).
DOI: https://doi.org/10.1016/j.jclepro.2021.126159

[2] B. Chen, S. Bao, Y. Zhang, Synergetic strengthening mechanism of ultrasound combined with calcium fluoride towards vanadium extraction from low-grade vanadium-bearing shal. International Journal of Mining Science and Technology **31** (6), 1095-1106 (2021). DOI: https://doi.org/10.1016/j.ijmst.2021.07.008

[3] B. Chen, S. Bao, Y. Zhang, L Ren, A novel and sustainable technique to precipitate vanadium from vanadium-rich solutions via efficient ultrasound irradiation. Journal of Cleaner Production **339**, 130755 (2022).
DOI: https://doi.org/10.1016/j.jclepro.2022.130755

[4] G. Yang, X. Sun, Z. Li, X. Li, Q. Yong, Effects of vanadium on the microstructure and mechanical properties of a high strength low alloy martensite steel. Materials and Design **50**, 102-107 (2013).
DOI: https://doi.org/10.1016/j.matdes.2013.03.019

[5] Q. Zhang, Y. Zhao, G. Yuan, W. Yang, The effect of vanadium on microstructure and mechanical properties of Fe-based high-strength alloy. Results in Physics **15**, 102335 (2019).
DOI: https://doi.org/10.1016/j.rinp.2019.102335

[6] C. Choi, S. Kim, R. Kim, Y. Choi, S. Kim, H. Jung, J. Yang, H. Kim, A review of vanadium electrolytes for vanadium redox flow batteries. Renewable and Sustainable Energy Reviews **69**, 263-274 (2017). https://doi.org/10.1016/j.rser.2016.11.188

[7] R. Moskalyk, A. Alfantazi, Processing of vanadium: a review. Minerals Engineering **16** (9), 793-805 (2003).
DOI: https://doi.org/10.1016/S0892-6875(03)00213-9

[8] J. Li, X. Zhou, M. Brochu, N. Provatas, Y. Zhao, Solidification microstructure simulation of Ti-6Al-4V in metal additive manufacturing: A review. Additive Manufacturing **31**, 1-14 (2020).
DOI: https://doi.org/10.1016/j.addma.2019.100989

[9] Q. Sun, L. Wang, R. Cheng, Z. Liu, X. He, N. Zhao, B. Liu, A Novel SiO_2-Supported Fluorine Modified Chromium-Vanadium Bimetallic Catalyst for Ethylene Polymerization and Ethylene/1-Hexene Copolymerizatio. Macromolecular Reaction Engineering **11** (5), 1600055 (2017).
DOI: https://doi.org/10.1002/mren.201600055

[10] W. Wang, Q. Luo, B. Li, X. Wei, L. Li, Z. Yang, Recent progress in redox flow battery research and development. Advanced Functional Materials **23** (8), 970-986 (2012).
DOI: https://doi.org/10.1002/adfm.201200694

[11] M. Skyllas-Kazacos, G. Kazacos, G. Poon, H. Verseema, Recent advances with UNSW vanadium-based redox flow batteries. International Journal of Energy Research **34** (2), 182-189 (2009).
DOI: https://doi.org/10.1002/er.1658

[12] M. Skyllas-Kazacos, L. Cao, M. Kazacos, N. Kausar, A. Mousa, Vanadium electrolyte studies for the vanadium redox battery-a review. ChemSusChem **9** (13), 1521-1543 (2016).
DOI: https://doi.org/10.1002/cssc.201600102

[13] Y. Wu, D. Chen, W. Liu, Z. Sun, B. Zhang, Global vanadium industry development report 2020. Iron Steel Vanadium Titanium **42** (5), 1-9 (2021) (In Chinese).
DOI: http://dx.doi.org/10.7513/j.issn.1004-7638.2021.05.001

[14] J. Xiang, Q. Huang, X. Lv, C. Extraction of vanadium from converter slag by two-step sulfuric acid leaching process. Journal of Cleaner Production **170**, 1089-1101 (2018).
DOI: https://doi.org/10.1016/j.jclepro.2017.09.255

[15] P. Taylor, S. Shuey, E. Vidal, J. Gomez, Extractive metallurgy of vanadium-containing titaniferous magnetite ores: a review. Mining, Metallurgy and Exploration **23**, 80-86 (2006).
DOI: https://doi.org/10.1007/BF03403340

[16] C. Lv, K. Yang, S. Wen, S. Bai, Q. Feng, A new technique for preparation of high-grade titanium slag from titanomagnetite concentrate by reduction-melting-magnetic separation processing. JOM **69**, 1801-1805 (2017).
DOI: https://doi.org/10.1007/s11837-017-2507-3

[17] H. Lv, M. Wu, Z. Zhang, X. Wu, L. Li, Z. Gao, Co-precipitation behaviour of titanium-containing silicate solution. Chemical Papers **70**, 1632-1641 (2016).
DOI: https://doi.org/10.1515/chempap-2016-0100

[18] J. He, X. Jiang, H. Ji, Y. Jin, Z. Zhang, F. Shen, Research progress on direct extraction of vanadium from vanadium titanium magnetite. China Metallurgy **33** (3), 29-38 (2023) (In Chinese).

[19] X. Luo, H. Dong, S. Zhang, Y. Liu, Study on the sodium oxidation properties of low-iron vanadium-titanium magnetite with

high vanadium and titanium. Energy Sources, Part A: Recovery, Utilization, and Environmental Effects **40** (17), 1998-2008 (2018). DOI: https://doi.org/10.1080/15567036.2018.1486907

[20] Y. Liu, F. Meng, F. Fang, W. Wang, J. Chu, T. Qi, Preparation of rutile titanium dioxide pigment from low-grade titanium slag pretreated by the NaOH molten salt method. Dyes and Pigments **125**, 384-391 (2016). DOI: https://doi.org/10.1016/j.dyepig.2015.10.036

[21] D. Chen, L. Zhao, Y. Liu, T. Qi, J. Wang, L. Wang, A novel process for recovery of iron, titanium, and vanadium from titanomagnetite concentrates: NaOH molten salt roasting and water leaching processes. Journal of Hazardous Materials **244-245**, 588-595 (2013). DOI: https://doi.org/10.1016/j.jhazmat.2012.10.052

[22] Y. Sui, Y. Guo, A. Travyanov, T. Jiang, F. Chen, G. Qiu, Reduction roasting-magnetic separation of vanadium tailings in presence of sodium sulfate and its mechanisms. Rare metals **35**, 954-960 (2016). DOI: https://doi.org/10.1007/s12598-015-0616-0

[23] Y. Zhang, L. Yi, L. Wang, D. Chen, W. Wang, Y. Liu, H. Zhao, T. Qi, A novel process for the recovery of iron, titanium, and vanadium from vanadium-bearing titanomagnetite: sodium modification–direct reduction coupled process. International Journal of Minerals Metallurgy and Materials, **24**, 504-511 (2017). DOI: https://doi.org/10.1007/s12613-017-1431-4

[24] Y. Luo, X. Che, X. Cui, Q. Zheng, L. Wang, Selective leaching of vanadium from V-Ti magnetite concentrates by pellet calcification roasting-H_2SO_4 leaching process. International Journal of Mining Science and Technology **31** (3), 507-513 (2021). DOI: https://doi.org/10.1016/j.ijmst.2021.02.002

[25] Z. Wang, Z. Peng, Y. Li, Y. Zhu, K. Xie, Selective sulfuric acid cyclic leaching of vanadium from the calcification roasting pellets of vanadium titanomagnetite. Journal of Materials Research and Technology **23**, 778-790 (2023). DOI: https://doi.org/10.1016/j.jmrt.2023.01.046

[26] F. Gao, H. Du, S. Wang, B. Chen, J. Li, Y. Zhang, M. Li, B. Liu, A.U. Olayiwola, A comparative study of extracting vanadium from vanadium titano-magnetite ores: Calcium salt roasting vs sodium salt roasting. Mineral Processing and Extractive Metallurgy Review **44** (5), 352-364 (2022). DOI: https://doi.org/10.1080/08827508.2022.2069105

[27] T. Wen, Y. Jiang, X. Liu, Extraction behavior of vanadium and chromium by calcification roasting-acid leaching from high chromium vanadium slag: optimization using response surface methodology. Metallurgy Review **40** (1), 56-66 (2018). DOI: https://doi.org/10.1080/08827508.2018.1481059

[28] M. Zhou, S. Yang, T. Jiang, Influence of MgO in form of magnesite on properties and mineralogy of high chromium, vanadium, titanium magnetite sinters. Ironmaking & Steelmaking **42** (3), 217-225. DOI: https://doi.org/10.1179/1743281214Y.0000000223

[29] W. Li, G. Fu, Q. Chu, Oxidation induration process and kinetics of Hongge vanadium titanium-bearing magnetite pellets. Ironmaking & Steelmaking **44** (4), 294-303. DOI: https://doi.org/10.1080/03019233.2016.1210751

[30] M. Zhou, S. Yang, T. Jiang, Influence of MgO in form of magnesite on properties and mineralogy of high chromium, vanadium, titanium magnetite sinters. Ironmaking & Steelmaking **42** (3), 217-225. DOI: https://doi.org/10.1179/1743281214Y.0000000223

[31] S. Munir, S. Daood, W. Nimmo, A. Cunliffe, B. Gibbs, Thermal analysis and devolatilization kinetics of cotton stalk, sugar cane bagasse and shea meal under nitrogen and air atmospheres. Bioresource Technology **100** (3), 1413-1418 (2009). DOI: https://doi.org/10.1016/j.biortech.2008.07.065

[32] M. Starink, A new method for the derivation of activation energies from experiments performed at constant heating rate. Thermochimica Acta **288** (1-2), 97-104 (1996). DOI: https://doi.org/10.1016/S0040-6031(96)03053-5

[33] S. Vyazovkin, C. Wight, Model-free and model-fitting approaches to kinetic analysis of isothermal and nonisothermal data. Thermochimica Acta **340-341**, 53-68 (1999). DOI: https://doi.org/10.1016/S0040-6031(99)00253-1

[34] J. Opfermann, E. Kaisersberger, H. Flammersheim, Model-free analysis of thermoanalytical data-advantages and limitations. Thermochimica Acta **391** (1-2), 119-127 (2002). DOI: https://doi.org/10.1016/S0040-6031(02)00169-7

[35] M. Starink, The determination of activation energy from linear heating rate experiments: a comparison of the accuracy of isoconversion methods. Thermochimica Acta **404** (1-2), 163-176 (2003). DOI: https://doi.org/10.1016/S0040-6031(03)00144-8

[36] P. Liu, C. Liu, S. Li, B. Liu, J. Shi, L. Zhang, J. Peng, Desorption Kinetic Study of Mercury Species in Spent Mercury Chloride Catalyst from Polyvinyl Chloride Production Process. Environmental Progress and Sustainable Energy **38** (5), 1-11 (2019). DOI: https://doi.org/10.1002/ep.13201

[37] A. Marini, V. Berbenni, G. Flor, Kinetic parameters from thermogravimetric data. Zeitschrift für Naturforschung A **34** (5), 661-663 (1979). DOI: https://doi.org/10.1515/zna-1979-0523

[38] A. Coats, J. Redfern, Kinetic parameters from thermogravimetric data. Nature **201**, 68-69 (1964). DOI: https://doi.org/10.1038/201068a0

[39] S. Vyazovkin, A. Burnham, J. Criado, L. Pérez-Maqueda, C. Popescu, N. Sbirrazzuoli, ICTAC Kinetics Committee recommendations for performing kinetic computations on thermal analysis data. Thermochimica Acta **520** (1-2), 1-19 (2011). DOI: https://doi.org/10.1016/j.tca.2011.03.034

[40] S. Vyazovkin, K. Chrissafis, M. Laura Di Lorenzo, N. Koga, M. Pijolat, B. Roduit, N. Sbirrazzuoli, J. Josep Suño, ICTAC Kinetics Committee recommendations for collecting experimental thermal analysis data for kinetic computations. Thermochimica Acta **590**, 1-23 (2014). DOI: https://doi.org/10.1016/j.tca.2014.05.036

[41] J. Elder, The general applicability of Kissinger equation in thermal analysis. Journal of Thermal Analysis **30**, 657-669 (1985). DOI: https://doi.org/10.1007/BF01913612

[42] T. Akahira, T. Sunose, Method of determining activation deterioration constant of electrical insulating materials. Res. Report Chiba Inst .Technol. **16**, 22-23 (1971).

[43] H. Zheng, Y. Sun, Y. Dong, Loss of vanadium and iron during calcification roasting-acid leaching of vanadium from vanadium titanomagnetite. Journal of Chemical Industry **66** (03), 1019-1025 (2015) (In Chinese).